JGR Space Physics

RESEARCH ARTICLE
10.1029/2020JA028856

Modulation of Magnetospheric Substorm Frequency: Dipole Tilt and IMF B_y Effects

A. Ohma[1], J. P. Reistad[1], and S. M. Hatch[1]

[1]Birkeland Centre for Space Science, University of Bergen, Bergen, Norway

Key Points:

- Substorms are more frequent when the dipole tilt angle and Interplanetary Magnetic Field B_y have opposite compared to equal sign
- This is a magnetospheric response, and cannot be explained by magnetosphere-ionosphere coupling affecting detection of substorms at ground
- Whether the combination of B_y and tilt angle affects the dayside reconnection rate or magnetotail processes is currently unresolved

Correspondence to:
A. Ohma,
anders.ohma@uib.no

Citation:
Ohma, A., Reistad, J. P., & Hatch, S. M. (2021). Modulation of magnetospheric substorm frequency: Dipole tilt and IMF B_y effects. *Journal of Geophysical Research: Space Physics*, *126*, e2020JA028856. https://doi.org/10.1029/2020JA028856

Received 22 OCT 2020
Accepted 26 JAN 2021

Abstract Substorm activity is heavily influenced by the Interplanetary Magnetic Field (IMF) B_z component and magnetospheric substorms occur most frequently when B_z is strongly negative. The substorm occurrence rate is also affected by the magnitude of the B_y component, but it is usually presumed that this contribution is independent of the sign of B_y. Using five independent substorm onset lists, we show that substorm activity does depend on the sign of B_y near the solstices. Specifically, we show that substorms occur more frequently when B_y and the dipole tilt angle Ψ have different signs as opposed to when they have the same sign. These results confirm that the magnetosphere exhibits an explicit dependence on the polarity of B_y for nonzero Ψ, as other recent studies have suggested, and imply variation in the dayside reconnection rate and/or the magnetotail response. On the other hand, we find no clear relationship between substorm intensity and B_y regardless of Ψ. Last, for the onset list based on identifying negative bays at auroral latitudes, we observe an overall trend of more frequent onsets for positive B_y, regardless of season. However, substorm frequency in the other four substorm lists does not exhibit an overall preference for positive B_y. We show that this phenomenon is very likely a consequence of the particular substorm identification method (i.e., identification of negative bays), which is affected by local ionospheric conditions that depend on B_y and Ψ.

Plain Language Summary The solar wind that the Sun continuously emits is a plasma with an embedded magnetic field. The direction in which this magnetic field points changes frequently, and is among the most important factors in controlling geomagnetic activity, or how frequent and how bright the aurorae are. From the perspective of an observer at the magnetic pole in the Northern Hemisphere, a downward-pointing solar wind magnetic field yields the highest amount of geomagnetic activity and results in frequent and bright auroral displays. The magnetic field can also have a "sideways" component that points either toward dawn or toward dusk. It is often assumed that geomagnetic activity does not depend on whether the magnetic field points toward dawn or dusk. In this study, we show that around each solstice this sideways component does matter. When Earth is tilted toward the Sun (northern summer/southern winter), a dawnward-pointing magnetic field gives more frequent auroral breakups than the other. When Earth is tilted away from the Sun, a duskward-pointing magnetic field yields more auroral breakups. This insight improves our understanding of how Earth is coupled to space.

1. Introduction

A magnetospheric substorm is a process where magnetic flux and energy stored in the magnetotail lobes are unloaded by reconnection in the near-Earth tail, causing a global reconfiguration of the magnetosphere (Hones, 1979; review by Baker et al., 1996). The shape of the magnetotail changes from a stretched configuration to a more dipolar configuration during the unloading, and a field-aligned current system, known as the substorm current wedge, develops near midnight (McPherron et al., 1973; review by Kepko et al., 2015). The current wedge closes in the ionosphere, leading to an enhancement of the westward electrojet. This enhancement causes a pronounced negative bay in the northward component of magnetometers in the auroral zone, a signature that is directly linked to the auroral substorm, as first described by Akasofu (1964). The auroral substorm starts with an onset, which is a sudden, localized brightening of the aurora, typically located at the equatorial boundary of the discrete aurora. The intensified region then expands, both longitudinally and poleward; this period of the substorm is referred to as the expansion phase. The expansion phase is followed by a recovery phase, in which the magnetospheric system slowly reverts toward its preonset

configuration. There are ongoing dynamics also in this substorm phase, for instance development of auroral omega bands (Opgenoorth et al., 1994).

Substorms are usually preceded by a growth phase (McPherron, 1970), a period associated with intervals of enhanced solar wind forcing, typically associated with southward Interplanetary Magnetic Field (IMF) (Borovsky & Yakymenko, 2017; Caan et al., 1977; Newell et al., 2013; Wild et al., 2009). The duration of this phase is typically 30–90 min (Li et al., 2013), during which magnetic flux and energy is loaded to the magnetosphere. Caan et al. (1975, 1978) performed superposed epoch analysis of the lobe magnetic field, centered at substorm onset. Their analysis showed that the magnetic energy and flux increase in the hours leading up to onset, and rapidly decrease in the hour after onset, confirming that loading of the open magnetosphere occurs in the period before a substorm. Consistent trends are found by e.g., Yamaguchi et al. (2004) and Coxon et al. (2018).

It is thus unsurprizing that the occurrence frequency of substorms depends on the upstream solar wind conditions. Kamide et al. (1977) showed that substorm activity becomes more frequent as the IMF becomes more southward. Substorms are also more frequent in the declining phase of the solar cycle (Borovsky & Yakymenko, 2017; Tanskanen, 2009) and during coronal mass ejection and high-speed streams as opposed to during slow solar wind conditions (Liou et al., 2018). Newell et al. (2013) demonstrated that the number of onsets per day correlates with a selection of solar wind coupling functions, but also directly with the solar wind velocity. However, the relationship between this coupling and the number of substorms is not necessarily linear, as the amount of flux closed by a substorm can also depend on the preceding solar wind-magnetosphere coupling.

Solar wind coupling functions aim to quantify the rate at with energy or magnetic flux is loaded into the magnetosphere through dayside reconnection. Over the last 50 years a variety of such coupling functions have been derived either from theoretical considerations or observations, or a combination of the two (e.g., Burton et al., 1975; McPherron et al., 2015; Milan et al., 2012; Newell et al., 2007; Perreault & Akasofu, 1978; Sonnerup, 1974; Tenfjord & Østgaard, 2013; Vasyliunas et al., 1982). The solar wind parameters used in these coupling functions are measured in Geocentric Solar Magnetic (GSM) coordinates, in which the x-axis points toward the Sun and the y-axis is perpendicular to the Sun-Earth line and the magnetic dipole axis, positive toward dusk. The z-axis completes the right-handed system. A few commonly used functions are $V_x B_s$ (Burton et al., 1975), $V_x^{4/3} B_{yz}^{2/3} \sin^{8/3}(\theta_{CA}/2)$ (Newell et al., 2007) and $\Lambda V_x^{4/3} B_{yz} \sin^{9/2}(\theta_{CA}/2)$ (Milan et al., 2012). Here, V_x is the x component of the solar wind velocity and $B_{yz} = \sqrt{B_y^2 + B_z^2}$, where B_y and B_z are the GSM components of the IMF. θ_{CA} is the IMF clock angle defined as $\arctan(B_y/B_z)$, and B_s is equal to B_z when $B_z < 0$ and zero when $B_z > 0$. The function estimated by Milan et al. (2012) also includes a scaling constant $\Lambda = 3.3\ 10^5\ \mathrm{m}^{2/3}\mathrm{s}^{1/3}$, making the unit of this function V = Wb/s, that is magnetic flux transport. Unless explicitly stated otherwise, IMF B_y (hereafter B_y) and θ_{CA} are calculated in GSM coordinates throughout this manuscript.

A common feature of the solar wind coupling functions is that they are symmetric with regard to the sign of B_y. Hence, it is presumed that only the magnitude of B_y plays a role in the dayside coupling. It has recently been documented, however, that certain aspects of the solar wind-magnetosphere-ionosphere coupling exhibit so-called explicit B_y effects. Although first pointed out by Friis-Christensen and Wilhjelm (1975); Holappa and Mursula (2018) further demonstrated and quantified the influence on the westward electrojet by the sign of B_y. They found that during local winter in the northern hemisphere, the AL index was ~50% greater for positive B_y compared to negative B_y, during otherwise similar conditions. The opposite trend was observed during local summer, where the AL index was ~20% greater for negative B_y. Consistent results were found using the K index of the Syowa station in the southern hemisphere, which is greater for positive B_y during local summer (northern winter) and greater for negative B_y during local winter (northern summer). The difference is also largest in the southern hemisphere during local winter. Similar seasonal differences in the AL index were shown by Friis-Christensen et al. (2017); Laundal et al. (2016) and have also been reported in Birkeland currents derived from the Average Magnetic field and Polar current Systems (AMPS) model (Laundal et al., 2018). Based on measurements from the dark hemisphere, Friis-Christensen et al. (2017) suggested that the strength of the westward electrojet in the substorm current wedge was modulated by B_y, appearing larger in the northern hemisphere for positive B_y and in the southern hemisphere for negative B_y.

In lieu of a satisfying explanation of the dependence of ionospheric currents on the polarity of B_y, further studies have revealed other aspects of the coupled solar wind-magnetosphere-ionosphere system that exhibit similar dependence on B_y polarity. Reistad et al. (2020) found that the average size of the Region 1/Region 2 (R1/R2) current system, approximated as the radius of a circle fitted to Active Magnetospheric and Planetary Electrodynamics Response Experiment (AMPERE) observations, was significantly different under positive and negative B_y. This difference was only evident when the Earth's dipole tilt angle Ψ (i.e., degree of tilt of the Earth's dipole axis along the Sun-Earth line) was large. By convention, $\Psi < 0$ corresponds to December solstice (northern winter/southern summer). Specifically, they found that for large, negative Ψ, positive B_y results on average in a slightly larger radius than negative B_y during otherwise similar conditions, as parameterized by a solar wind-magnetosphere coupling function (Milan et al., 2012). On the other hand, for large, positive Ψ (i.e., near June solstice) the radius of the R1/R2 current system has an opposite dependence on the sign of B_y. The same results were obtained from independent data in both hemispheres, which strongly suggests that this is not an effect of different magnetosphere-ionosphere (M-I) coupling in the two hemispheres, but is rather an effect of solar wind-magnetosphere interactions.

Holappa et al. (2020) recently reported a similar B_y polarity effect in the fluxes of high energy electron precipitation (>30 keV) in the auroral region, most notably in the midnight to morning local time sector. They found significantly larger fluxes during the same conditions for which Reistad et al. (2020) find a larger radius of the R1/R2 current system. Furthermore, their results are consistently seen in both hemispheres. Again, this strongly suggests that the cause of their observed asymmetry is not an effect of the different M-I coupling in the two hemispheres, but rather linked to a property of the solar wind-magnetosphere interactions during intervals of significant B_y and Ψ.

Liou et al. (2020) investigated substorm occurrence rates with special emphasis on the sign of B_y, also taking into account the level of upstream forcing. Their analysis indicated a trend of ∼30% more substorms during positive compared to negative B_y. However, Liou et al. (2020) only considered substorm lists based on detecting negative bays in the Small Cap 600 Index (*SML*) index (Newell & Gjerloev, 2011a), and did not sort their analysis with respect to dipole tilt or any other seasonal parameter. Here we demonstrate that both the underlying substorm signature used to identify onsets and seasonal parameters may influence the conclusions drawn from the analysis of substorm occurrence rates.

This study presents analysis of substorm occurrence rates from five independent lists of substorm onsets, all of which are sorted by IMF clock angle and dipole tilt angle. These lists and our methodology for processing them are described in the following section. We show the resulting onset frequency distributions in Section 3. We discuss the significance and physical implications of the results in Section 4, and summarize our findings in Section 5.

2. Data Processing

To determine how the substorm frequency depends on B_y and Ψ, we employ five substorm onset lists, each based on different onset signatures from independent data sets. Multiple lists are used to ensure that the observed trends are a signature of the magnetospheric response, and not the result of M-I coupling or the local conditions in the hemisphere where the observations are taken. The five substorm onset lists utilized in this study are introduced below.

1. A distinct aspect of substorms is a negative bay in ground magnetometers at auroral latitudes, caused by an enhancement of the westward electrojet. The *SML* index (Newell & Gjerloev, 2011a) quantifies the strength of the westward electrojet, and is based on ∼100 magnetometer stations at auroral latitudes in the northern hemisphere from the SuperMAG network of ground observatories (Gjerloev, 2012). Using an algorithm to identify sharp and sustained drops in the *SML* index, Newell and Gjerloev (2011a, 2011b), present an onset list (hereafter the N&G list) that consists of 70,278 onsets identified during 1981–2019
2. Positive bays in magnetometer data at mid-latitudes are a signature of field-aligned currents associated with the substorm current wedge. A mid-latitude positive bay (MPB) index using 41 ground magnetometers in both hemispheres (27 in the northern hemisphere and 14 in the southern hemisphere) was put forward by Chu et al. (2015); this index can be used to identify substorm onset by identifying bay signatures (Chu et al., 2015; McPherron & Chu, 2018). We have used the onset list described in McPherron

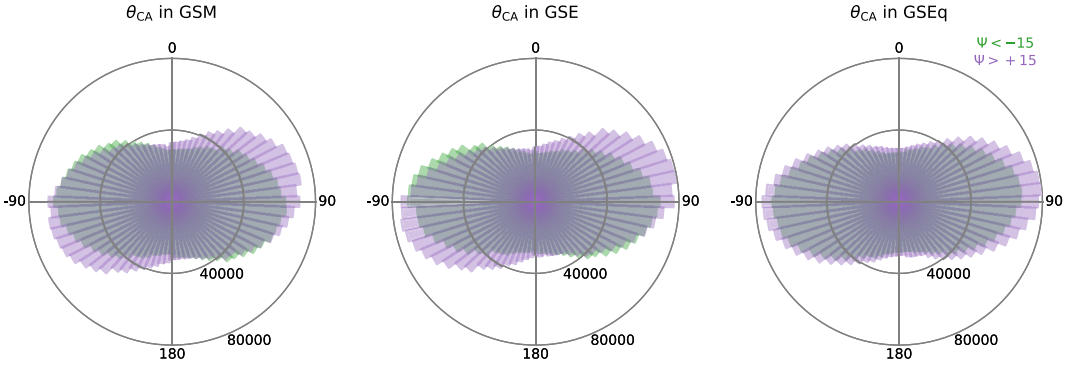

Figure 1. IMF clock angle distribution for $\Psi < -15°$ (green) and $\Psi > 15°$ (purple) in GSM (left), GSE (middle), and GSEq (right) coordinates. GSE, Geocentric Solar Ecliptic; GSEq, Geocentric Solar Equatorial; GSM, Geocentric Solar Magnetic.

and Chu (2018) (hereafter the McP&C list), which consists of 57,558 onsets in the years 1982–2012 when their proposed threshold value of the area of the positive bays, > 700 nT^2 ·min, is used

3. Another signature of substorm onset is Pi2 pulsations, which are oscillations in the geomagnetic field observed at low- and mid-latitudes. A related index, termed the Wave and planetary (Wp) index (World Data Center for Geomagnetism, Kyoto & Nosé, 2016), was proposed by Nosé et al. (2012). This index is based on 1 s magnetometer observations from 11 stations at low- and mid-latitudes in both hemispheres (8 in the northern hemisphere and 3 in the southern hemisphere), and is believed to reflect the wave power of the Pi2 pulsations. Nosé et al. (2012) also proposed threshold criteria for identifying substorm onsets from the Wp index. Using these criteria, we identify 14,075 onsets during 2005–2019 (hereafter the Nosé list)
4. Substorms are associated with a sudden, localized brightening of the aurora, which expands both longitudinally and poleward as the substorm progresses (Akasofu, 1964). We have used a combination of two onset lists based on global far-ultraviolet images of the aurora made by the IMAGE mission (Frey & Mende, 2006; Frey et al., 2004) and the Polar mission (Liou, 2010). These lists yield a combined total of 6,727 identified substorm onsets during 1996–2007. We refer to this combined list as the F + L list. Note that each list is based on images from a single orbiting spacecraft, which means that each spacecraft can only detect a substorm when it occurs within the field of view of the imaging instrument. Hence, this list does not provide full coverage of the given years. There are also three major data gaps in this data set; during July 3–December 3, 1996, during February 6–May 15, 2000 and during December 19, 2005–March 12, 2007. These periods are discarded in the analysis. About 1/3 of the IMAGE onsets and about 1/5 of the Polar onsets are from the southern hemisphere
5. Yet another signature of substorm onset is the injection of energetic electrons into geosynchronous orbit (Kamide & McIlwain, 1974; Weygand et al., 2008; Yeoman et al., 1994), which leads to a sharp drop in the specific entropy of the hot electron population (e.g., Borovsky & Cayton, 2011). Borovsky and Yakymenko (2017) present a substorm onset list (hereafter the B&Y list) based on identification of such drops using the Synchronous Orbit Particle Analyzer (SOPA) instrument on various geosynchronous spacecraft. The B&Y list is available at 30 min resolution, and gives 16,025 onsets in the years 1989–2007. Since the electron injection must drift to an orbiting spacecraft in order to be detected, the onsets determined by this method are systematically delayed by 0–30 min compared to the other lists. To account for this statistical bias, we have shifted the onsets in this list by −15 min. We nonetheless find that our results are nearly identical for delay times of 0, −15, and −30 min

Before comparing substorm occurrence rates, we identify a potential source of bias in this analysis and describe how we account for it. Figure 1 displays the distribution of the clock angle θ_{CA} during 1981–2019 in GSM coordinates, Geocentric Solar Ecliptic (GSE) coordinates and Geocentric Solar Equatorial (GSEq) coordinates for $\Psi < -15°$ and $\Psi > 15°$ using a bin size of 5°. These θ_{CA} values were calculated from the OMNI 1-min data, which is propagated to the nose of the Earth's bow shock (King & Papitashvili, 2005). Rotation

of the IMF vectors to GSEq coordinates were done with the aid of the International Radiation Belt Environment Modeling (IRBEM) library (Boscher et al., 2004–2008) using SpacePy 0.2.1 (Morley et al., 2011).

While the orientation of the two distributions are similar in GSEq coordinates, they are not similar in GSE and GSM coordinates; rather, they are rotated in opposite directions relative to the distributions in GSEq coordinates. For negative B_y, this apparent rotation corresponds to relatively more southward and less northward IMF for positive tilt angles compared to negative tilt angles, and vice versa for positive B_y. The distribution for $\Psi > 15°$ is quite asymmetric between negative and positive B_y in GSM coordinates, whereas the distribution for $\Psi < -15°$ is more symmetric. These changes in the orientation are the well-known Russell-McPherron effect (Russell & McPherron, 1973), which describes how mapping from GSEq coordinates to GSM coordinates leads to seasonal biases in the clock angle distribution, and hence different levels of geomagnetic activity depending on the IMF sector polarity (toward/away). The effect maximizes around equinoxes, but is also substantial near solstices. While the effect near equinoxes is due to the large angle between Earth's rotational axis and the normal of the ecliptic, the effect near solstice is due to the angle between the ecliptic and the Sun's equatorial plane. There are also more data for $\Psi > 15°$ compared to $\Psi < -15°$ (11.5%). About half of this difference is due to Earth's orbital motion; the duration from March equinox to September equinox is about 5 days longer than the duration from September equinox to March equinox and 5.5% more time is spent with $\Psi > 15°$ compared to $\Psi < -15°$ during 1981–2019. It is also worth noting that the IMF data is not divided equally between positive and negative clock angles, there is for instance a notably greater occurrence of positive compared to negative B_y for $\Psi > 15°$. These differences between the two clock angle distributions demonstrate that care must be taken when the number of substorms for the two polarities of B_y are compared for different tilt angle intervals.

Since the coupling between the IMF and terrestrial field is expected to be symmetric with regard to B_y and θ_{CA} in GSM coordinates only, we need to account for these season-related biases in the clock angle distribution rather than directly comparing the number of substorm onsets for negative and positive B_y. We account for these biases as follows. First, we divide the data into groups based on dipole tilt angle, Ψ, which was calculated using the method described in Laundal and Richmond (2017). We then bin the onsets by the average clock angle in GSM coordinates in the hour before each onset, and use the deciles of the absolute clock angle distribution during 1981–2019 to determine the bin size; this yields 10 bins containing approximately the same number of hours of data. We then normalize each clock angle bin by the number of days that the IMF clock angle has that particular range of orientations over the duration of each specific substorm list; thus each bin has units of substorm onsets per day. In order to estimate the uncertainty of the obtained frequencies, we apply bootstrapping on the time series in each bin. We draw 1,000 random samples (with replacement) from the time series, where each new sample has the same size as the original time series in that bin. From each sample we calculate the number of onsets per day, and the standard deviation of all the estimated onsets per day represents the standard error of the observed onset frequency.

3. Results

3.1. Onset Frequency

The distributions of substorm onsets per day are given in Figure 2. Each row corresponds to an independent substorm list, and each column corresponds to a different tilt angle interval. Blue and orange indicate negative and positive B_y, respectively. The numbers in the upper left corner of each panel are the total number of substorms for $\pm B_y$ identified by the onset identification method associated with that list, and the ratio of positive B_y to negative B_y onsets (black). The numbers in the lower right corner are the average number of substorms per day found by averaging the distributions in each panel, and the ratio of positive B_y to negative B_y onsets per day. These latter numbers are based on the binned data, in which biases in the clock angle distribution are accounted for.

From the figure, it is immediately clear that the distributions for positive and negative B_y are different for large tilt angles. For $\Psi < -15°$, there are more onsets per day for positive B_y than for negative B_y. This in most clear in the N&G list (top row), but consistently seen in all onset lists. The opposite effect is seen when $\Psi > 15°$, where there are more onsets per day for negative than positive B_y, again seen in all the list, albeit less pronounced in the N&G and McP&C lists. The effect is most notable for $45° < |\theta_{CA}| < 135°$, which is

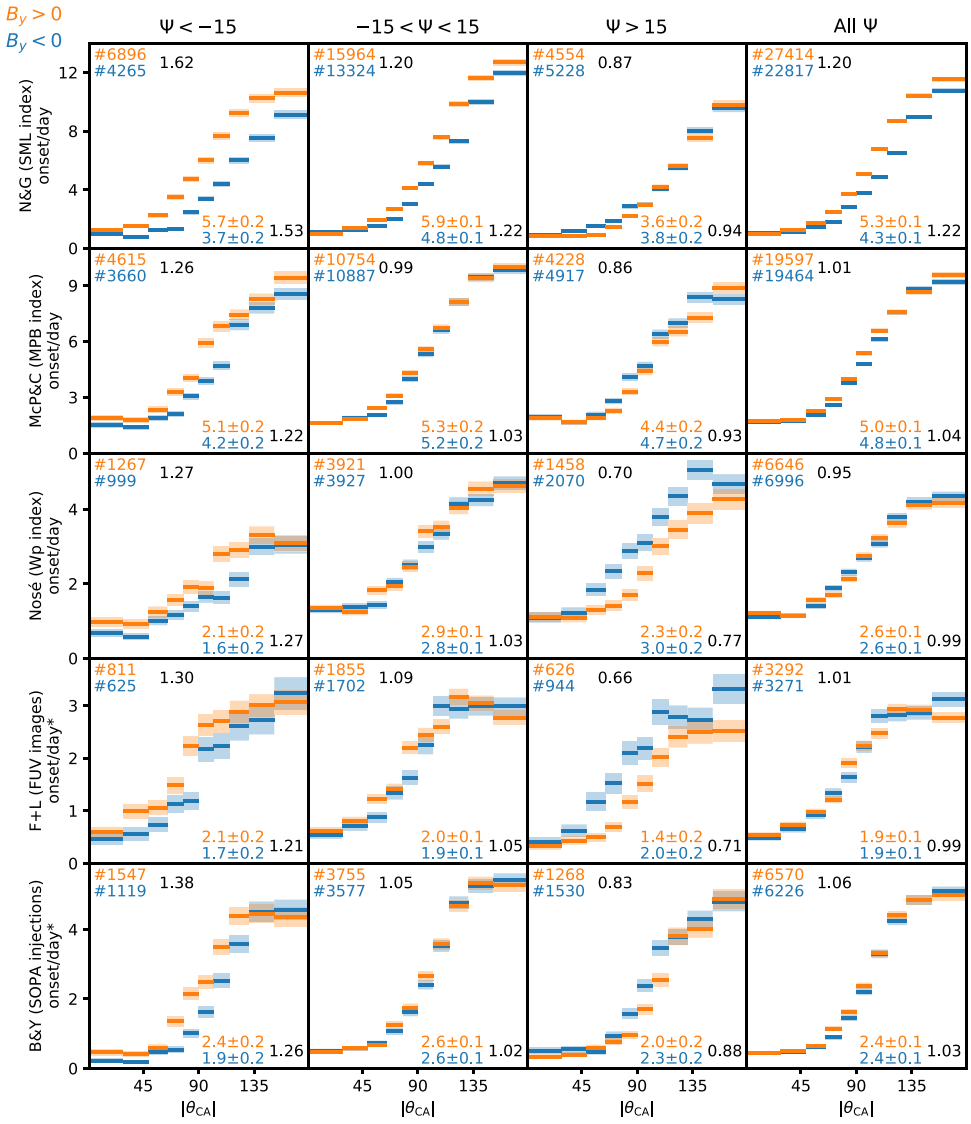

Figure 2. Onset occurrence rate for the five independent substorm onset lists. Blue colors indicate IMF $B_y < 0$ and orange colors indicate IMF $B_y > 0$. The numbers in the upper left corner of each panel are the number of onsets for $\pm B_y$, and the fraction of positive to negative onsets. The shading above and below each line indicates the standard error of the onset occurrence rate, estimated via the bootstrapping procedure described in the main text. The numbers in the lower right corner of each panel are the average number of substorms per day for $\pm B_y$, and the fraction of positive to negative onsets per day. The "*" symbol indicates lists based on spaceborne instruments, which do not have continuous coverage.

when B_y dominates. That most of the asymmetry in onset frequency remains after binning by clock angle (lower right in each panel), strongly suggests that nonzero dipole tilt modulates the substorm frequency, in addition to any asymmetry caused by the different clock angle distribution.

In the $|\Psi| < 15°$ tilt interval (second column) the distributions for $\pm B_y$ are similar and the average number of onsets per day about the same, with the notable exception of the N&G list, in which there are considerably more onsets for $B_y > 0$. In the rightmost column of the figure we show the two distributions that result when no restriction is placed on Ψ. These distributions are very similar to the $|\Psi| < 15°$ distributions, with very similar distributions for $\pm B_y$ for all lists except the N&G list. This discrepancy between the N&G list and the other onset lists will be addressed in Section 4.2.

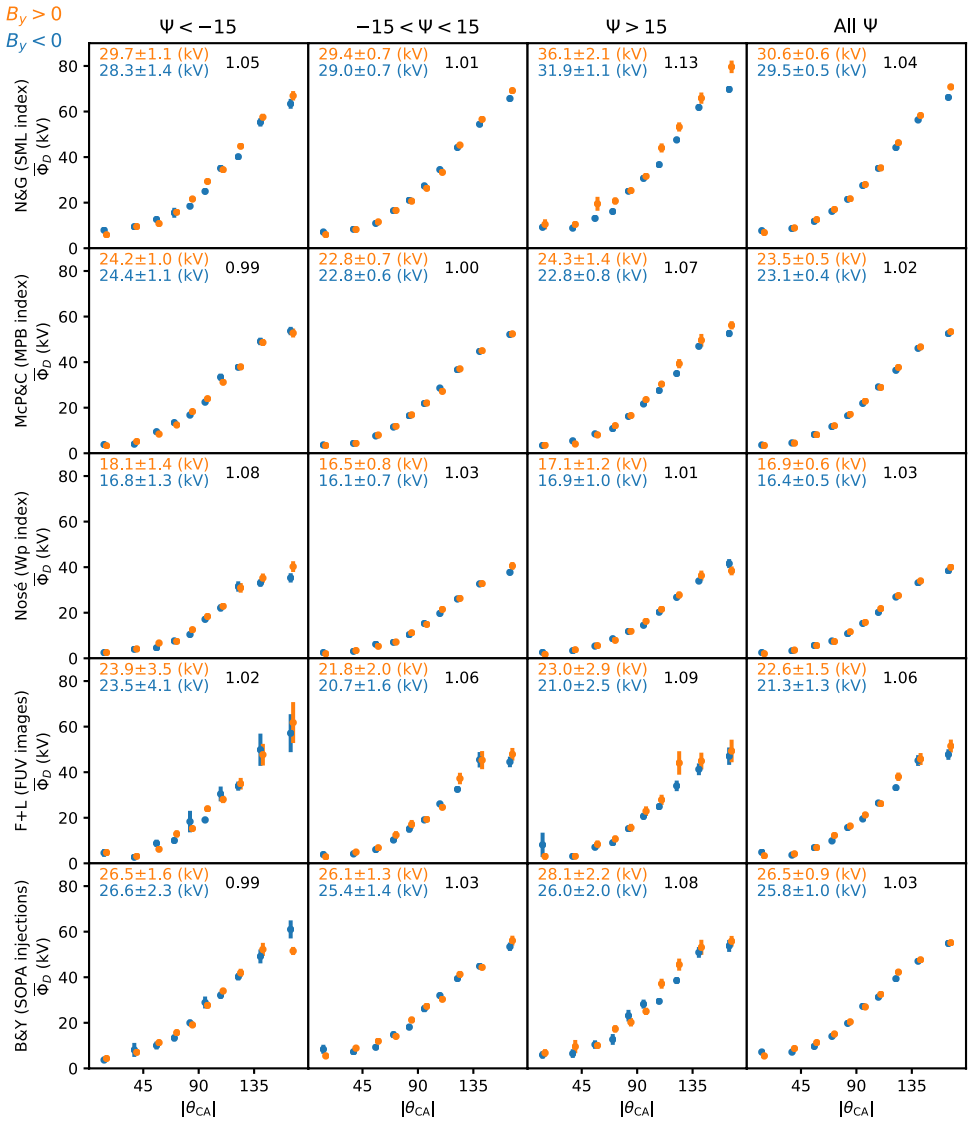

Figure 3. The mean solar wind forcing $\bar{\Phi}_D$ in each clock angle bin used in Figure 2 based on the mean solar wind forcing in the hour before each onset. Blue colors indicate $B_y < 0$ and orange colors indicate $B_y > 0$. The error bars indicate the standard error of the mean in each bin. The numbers are the mean and error of the binned values in each panel for $\pm B_y$, and the fraction of positive to negative solar wind forcing.

There appears to be a seasonal bias in the Nosé list, as the total number of substorms are significantly lower for $\Psi < -15°$ compared to $\Psi > 15°$ (middle row in Figure 2). Such bias is not apparent in any of the other lists, which instead indicate that the total number of onsets is about equal for large tilt angles. This bias could be a result of the local season in which the observations are obtained, as only 3 of 11 observatories are located in the southern hemisphere. However, the general trend for $\pm B_y$ in the list is in agreement with the observations from the other lists.

3.2. Solar Wind Forcing and Velocity

Potential biases in the solar wind forcing could influence the distributions in Figure 2, although a large portion of any such bias is already accounted for by binning on clock angle. Regardless, we have checked this by calculating the bin averages of the mean solar wind forcing in the hour before onset as estimated using the coupling function presented by Milan et al. (2012). In Figure 3, we estimate the average rate of flux opened

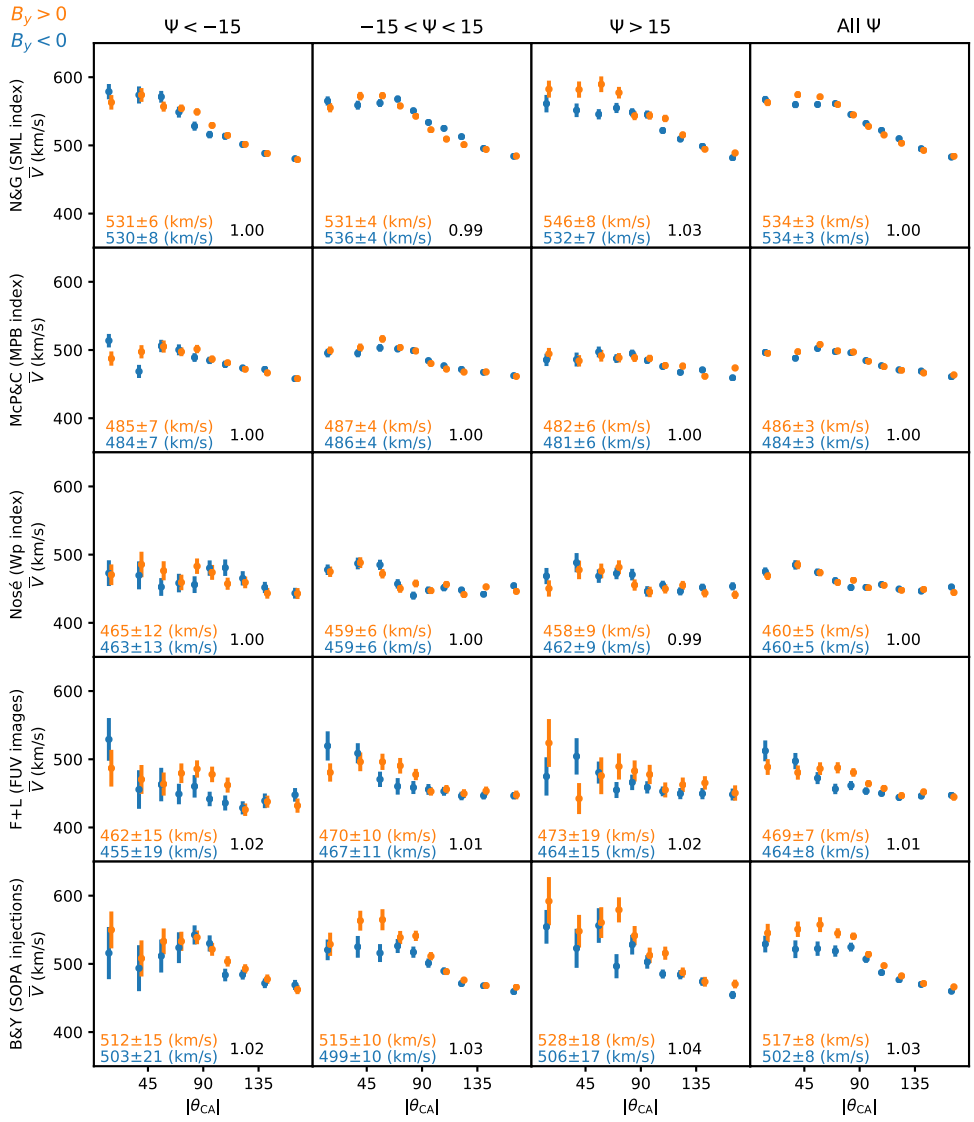

Figure 4. The mean solar wind speed $\bar{V}_{SW}$ in each clock angle bin used in Figure 2 based on the mean solar wind speed in the hour before each onset. Blue colors indicate $B_y < 0$ and orange colors indicate $B_y > 0$. The error bars indicate the standard error of the mean in each bin. The numbers are the mean and error of the binned values in each panel for $\pm B_y$, and the fraction of positive to negative velocities.

by dayside reconnection in the hour before onset via this coupling function for each identified substorm. We then calculate the bin averages in the same bins used in Figure 2. Blue indicates $B_y < 0$ and orange indicates $B_y > 0$, and the error bars display the standard error of the mean. The numbers in each panel indicate the average and error of the 10 data points in each panel for $\pm B_y$, and the fraction of positive to negative values. The figure shows that the solar wind coupling is about equal or a few percent larger for positive B_y, but show no systematic biases that could explain the observed onset trends in Figure 2. However, the weak trend of higher solar wind coupling observed for positive B_y could be the source of the slightly more pronounced trends seen for negative compared to positive Ψ, and the slightly higher onset rate for $B_y > 0$ when $|\Psi| < 15°$.

Newell et al. (2016) reported that the solar wind speed is the best predictor of substorm probability. Figure 4, which is in the same format as Figure 3, explores the role of the solar wind speed before each identified onset. For each substorm, we estimate the mean speed in the hour before substorm and then calculate the bin

averages. The values are very similar for $\pm B_y$, but slightly larger for $B_y > 0$ in the B&Y list. Again, we observe no underlying biases that could explain the onset trends in Figure 2.

3.3. IMF Stability

A final consideration is to address how sensitive the results in Figure 2 are to variations in the IMF orientation prior to onset. In order to quantify the stability of the IMF orientation, we calculate the circular variance in the hour before each onset, which for θ_{CA} can be defined as $\sigma = 1 - R = 1 - \sqrt{\langle \sin\theta_{CA} \rangle^2 + \langle \cos\theta_{CA} \rangle^2}$ where the angle brackets indicate the mean in the considered time interval. Geometrically $[\sin\theta_{CA}, \cos\theta_{CA}]$ defines the unit vector of the IMF component in the YZ_{GSM}-plane, which means that R is the magnitude of the mean unit vector. It can easily be shown that $R = 1$ if all the vectors point in exactly the same direction (constant θ_{CA}), yielding $\sigma = 0$. The value of R decreases as the vectors deviate from all pointing in a single direction and approaches zero for example, randomly or oppositely pointing IMF vectors. It follows that σ then approaches unity. This method has previously been used by for example, Haaland et al. (2007) and Ohma et al. (2019) to determine periods with stable IMF orientation.

Figure 5 displays the distributions of substorm onsets per day when only onsets and IMF data with $\sigma < 0.07$ are included in the analysis, which is the same limit as used by Ohma et al. (2019). To account for the reduced amount of data, we combine neighboring bins to a total of five bins; otherwise the figure is in the same format as Figure 2. The trends in Figure 5 are in agreement with the trends seen in Figure 2, thereby confirming the relationship between these trends and the corresponding clock angle orientations.

4. Discussion

The above analysis shows that the combination of dipole tilt and B_y modulate the occurrence frequency of substorm onset. We will elaborate on the significance and physical implications of the result, and discuss important differences among the lists, in the following sections.

4.1. An Explicit B_y Dependence for Large Tilt Angles

Despite being derived from independent data sources, the analysis of each of the five substorm lists shown in Figure 2 shows the same general trend: More frequent substorms when the sign of B_y and Ψ are opposite. The analysis thus reveals that the orientation of the dipole axis, together with the orientation of B_y, plays an important role in modulating the substorm onset frequency, which to our knowledge has not been shown earlier. The results in Figure 2 seem to complement those of Holappa et al. (2020), who found larger fluxes of high-energy electron precipitation in both hemispheres for opposite compared to equal sign of B_y and Ψ. The increased substorm frequency for opposite sign of the two parameters could explain the larger fluxes of high-energy electrons observed in the ionosphere, as high-energy precipitation is known to be sensitive to inner magnetospheric activations such as substorms (Beharrell et al., 2015). Hints of the effect in Figure 2 can also be seen in Borovsky and Yakymenko (2017), although it was not specifically called out by the authors. In their Table 2 and Figure 11, the occurrence rate of substorms is greater in the away sector during winter in the northern hemisphere and greater in the toward sector during summer in the northern hemisphere, both based on electron injections and *SML* jumps. The away and toward sectors of the IMF refers to whether the magnetic field in the Parker spiral point away from or toward the Sun, and is associated with positive and negative B_y, respectively.

The higher occurrence frequency of substorms for opposite compared to equal signs of B_y and Ψ can be interpreted in two ways: (1) Dayside opening of magnetic flux depends on the combination of B_y and Ψ; (2) The magnetotail responds differently to the same loading of magnetic flux for the different combinations of B_y and Ψ. We elaborate briefly on these two scenarios.

The shocked solar wind plasma, which interacts with the dayside magnetopause, has different properties in the prenoon and postnoon sectors due to the prevailing Parker spiral structure of the IMF. As shown by, for example, Walsh et al. (2014), the plasma β is typically larger in the prenoon magnetosheath plasma. These dawn-dusk asymmetries in the shocked solar wind plasma may affect the conditions for reconnection,

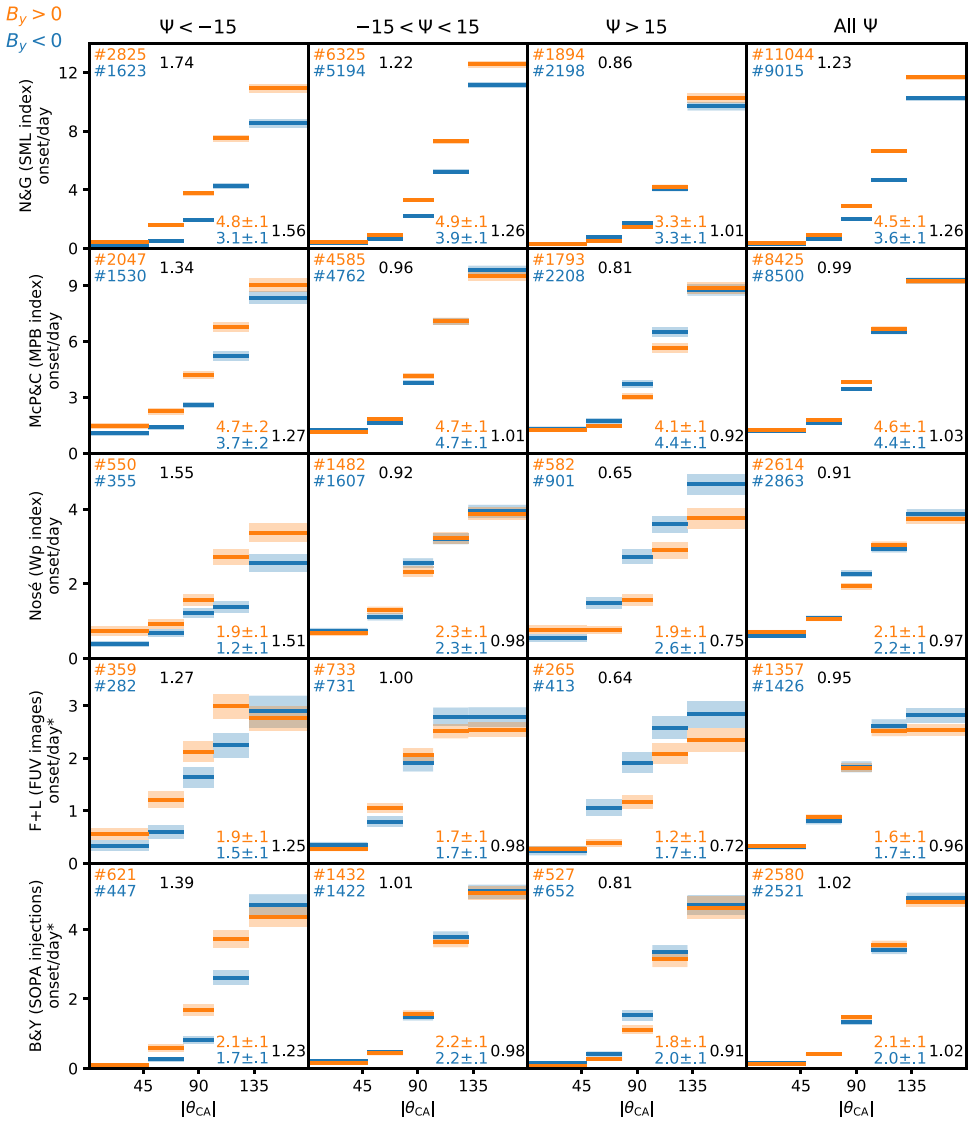

Figure 5. Onset occurrence rate for the five independent substorm onset lists with circular variance $\sigma < 0.07$. The figure has the same format as Figure 2 with the exception of fewer bins.

which is thought to be more effective in low-β regions (Cassak & Shay, 2007; Koga et al., 2019; Paschmann et al., 1986; review by Paschmann et al., 2013). The quasiparallel shock region (dawn) is also more prone than the quasiperpendicular region (dusk) to the development of Kelvin-Helmholtz-Instabilities (KHI) (Dimmock et al., 2016; Nosé et al., 1995; Nykyri et al., 2017). This leads to a dawn-favored plasma entry into the magnetosphere through reconnection inside the KHI vortices.

However, a dawn-dusk asymmetry is alone insufficient to explain putative B_y polarity effects on dayside reconnection, since the reconnection geometry for positive and negative B_y is mirror symmetric if $\Psi = 0°$. Therefore, although the reconnection rates might be different between the prenoon and postnoon sectors, the rates within each sector remain the same for both polarities of B_y when $\Psi = 0$. Thus, the total rate of flux opening is the same regardless of the polarity of B_y. This is consistent with the four onset lists showing little or no B_y polarity effect for small Ψ. This situation changes when Ψ is large. Under these conditions the two hemispheres are not symmetrically exposed to the solar wind and IMF, and differences can arise.

It is unfortunately not possible at present to relate substorm strength and frequency to changes in dayside reconnection rate. Not only is the fraction of flux closure through substorms to the opening of flux on the

dayside unknown, it may also depend on Ψ and B_y. Quantitative estimates of the degree of influence on the total dayside reconnection rate, including all the relevant physics, remain a theoretical and observational challenge.

An alternative explanation is that the tail responds differently for opposite and equal signs of B_y and Ψ. If we assume that the dayside reconnection rate is unaffected by the sign of B_y, the same amount of flux is added to the magnetosphere for $\pm B_y$. This means that the same amount of flux must, at some point, close again in the tail. Since the observed substorm frequency does vary with B_y polarity and dipole tilt, this could either mean that the average amount of flux closed by the substorms also differs (e.g., more frequent and weaker substorms for B_y and Ψ with opposite signs, and less frequent and stronger substorms for B_y and Ψ with the same sign), that substorms are more prone to lead to steady magnetospheric convection (SMC) (Sergeev et al., 1996) for one combination that the other, or that the flux throughput is accommodated without initiating substorms.

While we do not conjecture why the tail should respond differently, it is in any case known that the geometry of the closed tail is influenced both by Ψ and B_y. It is possible that a combination of plasma sheet warping for $\Psi \neq 0$ (Fairfield, 1980; Russell & Brody, 1967; Tsyganenko & Fairfield, 2004) and plasma sheet rotation when $B_y \neq 0$ (Cowley, 1981; Liou & Newell, 2010) causes different conditions for tail reconnection and substorm activation in the premidnight sector, where substorms are preferably initiated (Frey et al., 2004; Grocott et al., 2010; Liou, 2010). It has also been shown by Milan et al. (2019) that high-latitude onsets are more prone to develop into SMC events, whereas low-latitude onsets experience convection-breaking (Grocott et al., 2009) that leads to loading-unloading cycles. Furthermore, the average size of the polar cap is expanded for opposite compared to equal sign of B_y and Ψ (Reistad et al., 2020); this effect might also influence the substorm occurrence rates.

4.2. Are Substorms Generally More Frequent for Positive B_y?

Recently, Liou et al. (2020) reported that substorms are generally more frequent (and stronger) for positive compared to negative B_y, regardless of season. Using the N&G onset list, which is based on identifying negative bays in the *SML* index, and taking into account the level of upstream solar wind forcing, they report that substorms are about 30% more common for positive compared to negative B_y. The same trend is found for in our analysis, as seen in the top row of Figure 2. Both for small tilt angles and when we do not impose a restriction on dipole tilt angle we observe 22% more onsets for $B_y > 0$ compared to $B_y < 0$. Similar trends are also seen in other onset lists based on the *SML* index (Borovsky & Yakymenko, 2017; Forsyth et al., 2015, not shown). However, this trend is not observed for any of the other lists. It is therefore necessary to address why the onset distributions based on negative bays in the auroral electrojet in the northern hemisphere deviates from the distributions based on other onset signatures, are substorms in fact more common for positive compared to negative B_y, or is this trend related to some other physical conditions affecting the detection differently for $\pm B_y$?

If global magnetospheric substorms are generally more frequent and stronger for positive B_y, the effect should be observed in both the northern and southern hemisphere. To address this point, we perform a superposed epoch analysis based on data from both hemispheres. For the northern hemisphere we use the standard *SML* index, which is based on magnetometers with magnetic latitude between 40 and 80°. For the southern hemisphere we have compiled a corresponding *SML** index, which is based on all available SuperMAG magnetometers with magnetic latitude between −40° and −80°. We strongly emphasize that the magnetometers in the southern hemisphere are few and unevenly distributed, and quantitative comparison to the northern hemisphere counterpart is probably not warranted. However, the analysis can yield a qualitative description of any differences in the response between the hemispheres.

Figure 6 displays the superposed epoch analysis of the *SML* index (top) and the *SML** index (bottom), centered at substorm onsets identified by McP&C, during 1994–2012. This analysis includes only substorm onsets for which the average clock angle in the hour before onset is in the interval $45° < |\theta_{CA}| < 135°$. Each column corresponds to a different dipole tilt interval. Blue and orange indicate negative and positive B_y, respectively, and the shaded area indicates the standard error of the mean. The numbers in the upper right

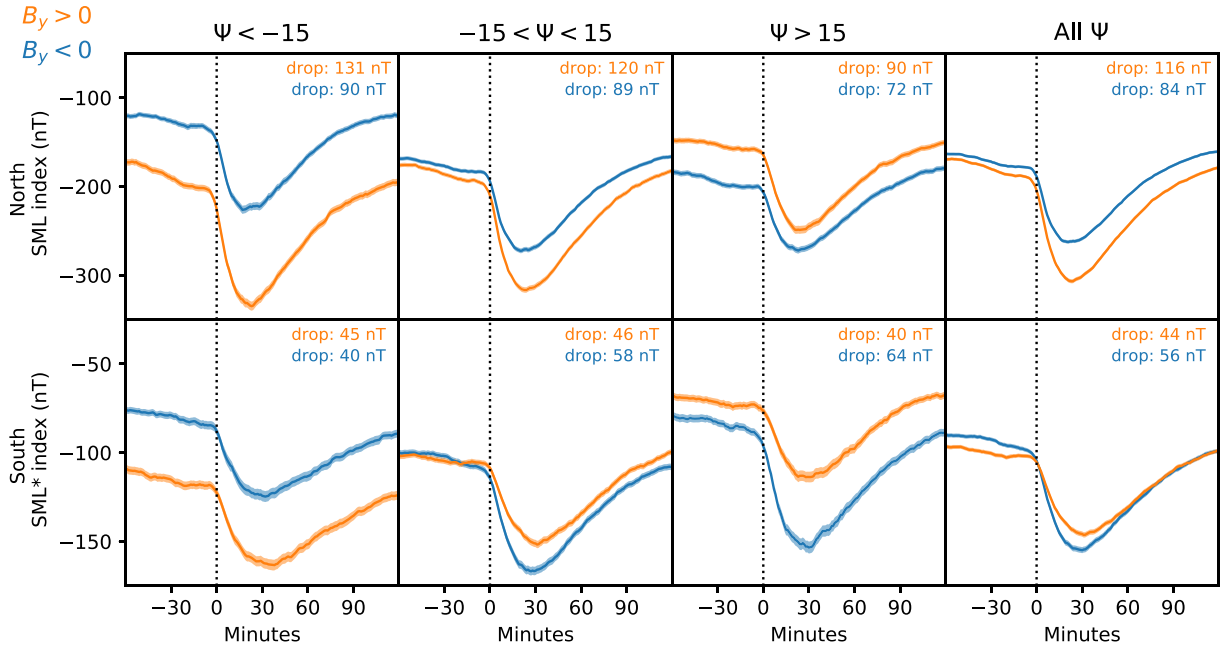

Figure 6. Superposed epoch analysis of the *SML* index based on magnetometers in the northern hemisphere (top) and a compiled *SML** index based on magnetometers in the southern hemisphere (bottom) during 1994–2012. Zero epoch corresponds to substorm onset in the McP&C list. Blue and orange indicate negative and positive B_y, respectively. Only onsets for which the average clock angle in the hour before onset is in the interval $45° < |\theta_{CA}| < 135°$ are included. SML, Small Cap 600 Index.

corner indicate the drop for each curve. This value was determined by subtracting the minimum values from the maximum value near onset (±5 min).

For the *SML* index in the northern hemisphere, we observe an opposite trend for $\pm B_y$ when Ψ is large; the average curve for positive B_y is below the average curve for negative B_y when $\Psi < -15°$, and vice versa for $\Psi > 15°$. The trend is more pronounced for $\Psi < -15°$. For the *SML** index we observe the same trends; the average curve for positive B_y is below the average curve for negative B_y when $\Psi < -15°$, and vice versa for $\Psi > 15°$, also in the southern hemisphere. These observations are in agreement with the monthly averages of the *AL* index (northern hemisphere) and the *K* index of the Japanese Syowa station (southern hemisphere) presented by Holappa and Mursula (2018). This illustrates the global nature of the explicit B_y effect, yielding a stronger westward electrojet for opposite compared to equal sign of B_y and Ψ in both hemispheres. The perturbations in Figure 6 are much weaker in the southern hemisphere than in the northern hemisphere, but this is expected as the average distance from the substorm current system to the ground stations is much larger there. Despite this difference, the general trends observed are remarkably consistent between the hemispheres when the sign of B_y and Ψ is reversed.

For $|\Psi| < 15°$ and for all Ψ (second and rightmost columns), opposite trends are observed in the two hemispheres. The negative bays in the *SML* index are more pronounced for $B_y > 0$, with a sharper and deeper drop, in both subsets. This is consistent with Liou et al. (2020), who find a general trend of more frequent and stronger substorms for positive B_y. However, the negative bays in the *SML** index are more pronounced for negative B_y (larger drop). Since this particular response in Figure 6 is opposite in the southern and northern hemisphere, it cannot represent a global difference between positive and negative B_y. Rather, it indicates that the difference is due to conditions in the local hemisphere. We suggest that the geometry of high-latitude current systems causes these trends, which varies drastically with the sign of B_y. The geometry of the current systems is, however, expected to be approximately equal in the two hemispheres if the sign of B_y and Ψ is reversed. This is consistent with the trends in Figure 6.

Regardless of the exact source of the discrepancy between positive and negative B_y, the trends in Figure 6 illustrate how any algorithm designed to identify sharp and/or sustained drops in auroral electrojet-based indices from the northern hemisphere is more prone to detect onsets for $B_y > 0$ compared to $B_y < 0$. If the

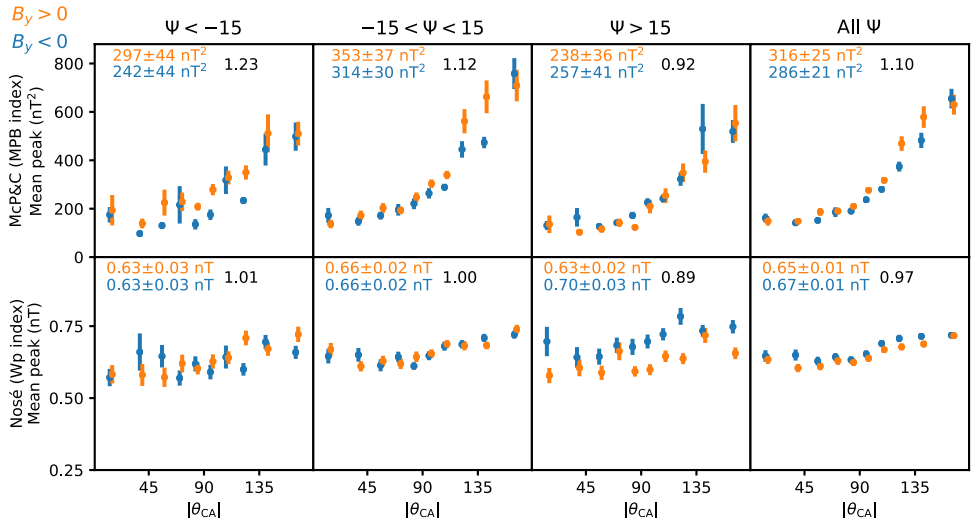

Figure 7. The mean peak value of the MPB index for the McP&C onsets (top) and the mean peak value of the Wp index for the Nosé onsets (bottom) in each clock angle bin used in Figure 2. Blue colors indicate $B_y < 0$ and orange colors indicate $B_y > 0$. The error bars indicate the standard error of the mean in each bin and the numbers are the mean and error of the binned values in each panel for $\pm B_y$. MPB, midlatitude positive bay; Wp, Wave and planetary.

spatial coverage of magnetometers in the southern hemisphere had allowed, these results suggest that the opposite would have been seen in an onset list based on southern hemispheric observations. Additionally, none of the other onsets lists observe a large general trend of higher onset frequency for the two B_y polarities, either during small dipole tilt conditions or when no restriction on the dipole tilt angle is imposed. These lists are also more robust with regards to local ionospheric conditions affecting the detection differently for $\pm B_y$, as they are either based on observations from both hemispheres (McP&C, Nosé and F + L) or obtained in the magnetosphere (B&Y). Hence, in contrast to (Liou et al., 2020), we conclude that there is no strong general trend toward more substorms when B_y is positive compared to negative, regardless of the dipole tilt orientation. If any such effect exists, its influence on the daily rate of substorm occurrence is relatively minor, and no larger than a few percent.

4.3. Do the Combination of B_y and Dipole Tilt Affect Substorm Intensity?

It is relevant to address whether or not substorm intensity is affected by the sign of B_y for large tilt angles. One option would have been to consider the magnitude of the *SML* index, but as shown in the previous section, the difference between positive and negative B_y is considerably affected by local ionospheric conditions. The magnitude of the *SML* index can therefore not be used to compare the intensity of substorms under different B_y conditions. Due to the few and unevenly distributed magnetometers in the southern hemisphere, any quantitative comparison between the two hemispheres is difficult. We have therefore considered two other alternatives.

The McP&C onset list provides several parameters describing each positive bay: peak value, area and duration of each pulse, as quantified by the MPB index (Chu et al., 2015). We have considered the peak values, which corresponds to the maximum power of the magnetic perturbations at mid-latitudes caused by the substorm current wedge, but similar trends are also seen for the Bay area and when we subtract the baseline value of the MPB index based on the start and end values of each peak. The mean peak value of all McP&C onsets within each bin used in Figure 2 is shown in the top row of Figure 7. The error bars indicate the standard error of the mean in each bin and the numbers are the mean and error of the binned values in each panel for $\pm B_y$. We observe higher mean peaks for positive B_y when $\Psi < -15°$ and weak indications of higher peaks for negative B_y when $\Psi > 15°$. There is also a weak trend of higher mean peaks for $|\Psi| < 15°$, and when we put no restriction on Ψ. However, neither trend is statistically significant.

The magnitude of the Wp index can be regarded as the average amplitude of nightside Pi2 pulsation (Nosé et al., 2012), which again correlates with auroral power (Takahashi & Liou, 2004; Takahashi et al., 2002). We have therefore found the maximum value of the Wp index in the 20 min following each Nosé onset. The mean of these peak values are shown in the bottom row in Figure 7, again using the same bins as in Figure 2. While we observe no systematic or significant difference between positive and negative B_y for $\Psi < -15°$ and $|\Psi| < 15°$, the values are significantly larger for negative B_y when $\Psi > 15°$. The same is seen when we put no restriction on Ψ, but this is most likely just a reflection of the difference in substorm occurrence rate seen in Figure 2, leading to a bias toward positive tilt angles.

Based on the combined results in Figure 7, we see either no difference for $\pm B_y$, or a weak signature of higher substorm intensity for opposite compared to equal sign of B_y. Hence, there is no indication that substorms are stronger and less frequent for equal sign of B_y and Ψ. However, as the values reported here are proxies of the substorm intensity, and do not directly measure either dissipated energy or closure of magnetic flux, the evidence presented here is only suggestive.

5. Summary

Using five independent substorm onset lists, we have shown that the substorm frequency depends on the sign of IMF B_y when the Earth's dipole tilt angle is large. Specifically, we find a higher substorm frequency when B_y and Ψ have opposite compared to equal signs. Since substorms are a global, magnetospheric process, this confirms that substorm-related magnetospheric processes explicitly depend on the polarity of B_y. We have outlined possible physical mechanisms, and pointed out the present lack of a coherent understanding of these processes. This should encourage further research effort into determining why some magnetospheric processes depend explicitly on the sign of B_y. When we consider substorm intensity, we find no clear relationship between substorm intensity and the sign of B_y and Ψ. Substorm intensity appears to be unchanged or only weakly enhanced for opposite sign of B_y and Ψ.

With the exception of one onset list that is based on identifying negative bays in the westward electrojet, we find little or no difference in the substorm frequency for $\pm B_y$ for small tilt angles or when we do not impose a restriction on dipole tilt angle. We therefore conclude that the magnetosphere only exhibits the explicit B_y effect when the dipole tilt is large, and that the general trend of more frequent onsets for $B_y > 0$ compared to $B_y < 0$ observed in the N&G list is a result on the ionospheric conditions and not the magnetospheric response.

Data Availability Statement

The OMNI solar wind data were downloaded from https://cdaweb.gsfc.nasa.gov/sp_phys/data/omni/hro_1min/. The *SML* index, N&G list and superMAG data were downloaded from http://supermag.jhuapl.edu. The Wp index, from which we derived the Nosé list, was downloaded from http://www.isee.nagoya-u.ac.jp/~nose.masahito/s-cubed/. The IMAGE FUV onsets were obtained from http://sprg.ssl.berkeley.edu/image/.

Acknowledgments
This study was supported by the Research Council of Norway/CoE under contract 223252/F50. We gratefully acknowledge the SuperMAG collaborators (http://supermag.jhuapl.edu/info/?page=acknowledgement). We thank K. M. Laundal for providing software to calculate the dipole tilt angle (https://github.com/klaundal/dipole).

References

Akasofu, S.-I. (1964). The development of the auroral substorm. *Planetary and Space Science*, *12*(4), 273–282. https://doi.org/10.1016/0032-0633(64)90151-5

Baker, D. N., Pulkkinen, T. I., Angelopoulos, V., Baumjohann, W., & McPherron, R. L. (1996). Neutral line model of substorms: Past results and present view. *Journal of Geophysical Research*, *101*(A6), 12975–13010. https://doi.org/10.1029/95JA03753

Beharrell, M. J., Honary, F., Rodger, C. J., & Clilverd, M. A. (2015). Substorm-induced energetic electron precipitation: Morphology and prediction. *Journal of Geophysical Research: Space Physics*, *120*(4), 2993–3008. https://doi.org/10.1002/2014JA020632

Borovsky, J. E., & Cayton, T. E. (2011). Entropy mapping of the outer electron radiation belt between the magnetotail and geosynchronous orbit. *Journal of Geophysical Research*, *116*(A6), A06216. https://doi.org/10.1029/2011JA016470

Borovsky, J. E., & Yakymenko, K. (2017). Substorm occurrence rates, substorm recurrence times, and solar wind structure. *Journal of Geophysical Research: Space Physics*, *122*(3), 2973–2998. https://doi.org/10.1002/2016JA023625

Boscher, D., Bourdarie, S., O'Brien, P., & Guild, T. (2004–2008). *Irbem library v4. 3, 2004–2008*. ONERA-DESP, Toulouse France, Aerospace Corporation, Washington, DC. Retrieved from https://sourceforge.net/projects/irbem/

Burton, R. K., McPherron, R. L., & Russell, C. T. (1975). An empirical relationship between interplanetary conditions and Dst. *Journal of Geophysical Research*, *80*(31), 4204–4214. https://doi.org/10.1029/JA080i031p04204

Caan, M. N., McPherron, R. L., & Russell, C. T. (1975). Substorm and interplanetary magnetic field effects on the geomagnetic tail lobes. *Journal of Geophysical Research*, *80*(1), 191–194. https://doi.org/10.1029/JA080i001p00191

Caan, M. N., McPherron, R. L., & Russell, C. T. (1977). Characteristics of the association between the interplanetary magnetic field and substorms. *Journal of Geophysical Research*, *82*(29), 4837–4842. https://doi.org/10.1029/JA082i029p04837

Caan, M. N., McPherron, R. L., & Russell, C. T. (1978). The statistical magnetic signature of magnetospheric substorms. *Planetary and Space Science*, *26*(3), 269–279. https://doi.org/10.1016/0032-0633(78)90092-2

Cassak, P. A., & Shay, M. A. (2007). Scaling of asymmetric magnetic reconnection: General theory and collisional simulations. *Physics of Plasmas*, *14*(10), 102114. https://doi.org/10.1063/1.2795630

Chu, X., McPherron, R. L., Hsu, T.-S., & Angelopoulos, V. (2015). Solar cycle dependence of substorm occurrence and duration: Implications for onset. *Journal of Geophysical Research: Space Physics*, *120*(4), 2808–2818. https://doi.org/10.1002/2015JA021104

Cowley, S. W. H. (1981). Magnetospheric asymmetries associated with the Y-component of the IMF. *Planetary and Space Science*, *29*(1), 79–96. https://doi.org/10.1016/0032-0633(81)90141-0

Coxon, J. C., Freeman, M. P., Jackman, C. M., Forsyth, C., Rae, I. J., & Fear, R. C. (2018). Tailward propagation of magnetic energy density variations with respect to substorm onset times. *Journal of Geophysical Research: Space Physics*, *123*(6), 4741–4754. https://doi.org/10.1029/2017JA025147

Dimmock, A. P., Nykyri, K., Osmane, A., & Pulkkinen, T. I. (2016). Statistical mapping of ULF Pc3 velocity fluctuations in the Earth's dayside magnetosheath as a function of solar wind conditions. *Advances in Space Research*, *58*(2), 196–207. https://doi.org/10.1016/j.asr.2015.09.039

Fairfield, D. (1980). A statistical determination of the shape and position of the geomagnetic neutral sheet. *Journal of Geophysical Research*, *85*(A2), 775–780. https://doi.org/10.1029/JA085iA02p00775

Fisher, N. I. (1993). *Statistical analysis of circular data*. Cambridge: Cambridge University Press. https://doi.org/10.1017/CBO9780511564345

Forsyth, C., Rae, I. J., Coxon, J. C., Freeman, M. P., Jackman, C. M., Gjerloev, J., et al. (2015). A new technique for determining Substorm Onsets and Phases from Indices of the Electrojet (SOPHIE). *Journal of Geophysical Research: Space Physics*, *120*(12), 10592–10606. https://doi.org/10.1002/2015JA021343

Frey, H. U., & Mende, S. B. (2006). Substorm onsets as observed by IMAGE-FUV. In *Proceedings of the 8th international conference on substorms* (pp. 71–76).

Frey, H. U., Mende, S. B., Angelopoulos, V., & Donovan, E. F. (2004). Substorm onset observations by IMAGE-FUV. *Journal of Geophysical Research*, *109*(A10), A10304. https://doi.org/10.1029/2004JA010607

Friis-Christensen, E., Finlay, C. C., Hesse, M., & Laundal, K. M. (2017). Magnetic Field Perturbations from Currents in the Dark Polar Regions During Quiet Geomagnetic Conditions. *Space Science Reviews*, *206*(1–4), 281–297. https://doi.org/10.1007/s11214-017-0332-1

Friis-Christensen, E., & Wilhjelm, J. (1975). Polar cap currents for different directions of the interplanetary magnetic field in the Y-Z plane. *Journal of Geophysical Research*, *80*(10), 1248–1260. https://doi.org/10.1029/JA080i010p01248

Gjerloev, J. W. (2012). The supermag data processing technique. *Journal of Geophysical Research*, *117*(A9), A09213. https://doi.org/10.1029/2012JA017683

Grocott, A., Milan, S. E., Yeoman, T. K., Sato, N., Yukimatu, A. S., & Wild, J. A. (2010). Superposed epoch analysis of the ionospheric convection evolution during substorms: IMF BY dependence. *Journal of Geophysical Research*, *115*(A5), A00106. https://doi.org/10.1029/2010JA015728

Grocott, A., Wild, J. A., Milan, S. E., & Yeoman, T. K. (2009). Superposed epoch analysis of the ionospheric convection evolution during substorms: Onset latitude dependence. *Annales Geophysicae*, *27*(2), 591–600. https://doi.org/10.5194/angeo-27-591-2009

Haaland, S. E., Paschmann, G., Förster, M., Quinn, J. M., Torbert, R. B., McIlwain, C. E., et al. (2007). High-latitude plasma convection from Cluster EDI measurements: method and IMF-dependence. *Annales Geophysicae*, *25*(1), 239–253. https://doi.org/10.5194/angeo-25-239-2007

Holappa, L., Asikainen, T., & Mursula, K. (2020). Explicit IMF dependence in geomagnetic activity: Modulation of precipitating electrons. *Geophysical Research Letters*, *47*(4), e2019GL086676. https://doi.org/10.1029/2019GL086676

Holappa, L., & Mursula, K. (2018). Explicit IMF by dependence in high-latitude geomagnetic activity. *Journal of Geophysical Research: Space Physics*, *123*(6), 4728–4740. https://doi.org/10.1029/2018JA025517

Hones, E. W. (1979). Plasma flow in the magnetotail and its implications for substorm theories. In S.-I. Akasofu (Ed.), Dynamics of the magnetosphere. Vol. 78 (pp. 545–562). Dordrecht: Springer Netherlands. https://doi.org/10.1007/978-94-009-9519-2_29

Kamide, Y., & McIlwain, C. E. (1974). The onset time of magnetospheric substorms determined from ground and synchronous satellite records. *Journal of Geophysical Research*, *79*(31), 4787–4790. https://doi.org/10.1029/JA079i031p04787

Kamide, Y., Perreault, P. D., Akasofu, S. I., & Winningham, J. D. (1977). Dependence of substorm occurrence probability on the interplanetary magnetic field and on the size of the auroral oval. *Journal of Geophysical Research*, *82*(35), 5521–5528. https://doi.org/10.1029/JA082i035p05521

Kepko, L., McPherron, R. L., Amm, O., Apatenkov, S., Baumjohann, W., Birn, J., et al. (2015). Substorm current wedge revisited. *Space Science Reviews*, *190*(1–4), 1–46. https://doi.org/10.1007/s11214-014-0124-9

King, J. H., & Papitashvili, N. E. (2005). Solar wind spatial scales in and comparisons of hourly wind and ace plasma and magnetic field data. *Journal of Geophysical Research*, *110*(A2), A02104. https://doi.org/10.1029/2004JA010649

Koga, D., Gonzalez, W. D., Souza, V. M., Cardoso, F. R., Wang, C., & Liu, Z. K. (2019). Dayside Magnetopause Reconnection: Its dependence on solar wind and magnetosheath conditions. *Journal of Geophysical Research: Space Physics*, *124*(11), 8778–8787. https://doi.org/10.1029/2019JA026889

Laundal, K. M., Finlay, C. C., Olsen, N., & Reistad, J. P. (2018). Solar wind and seasonal influence on ionospheric currents from Swarm and CHAMP measurements. *Journal of Geophysical Research: Space Physics*, *123*(5), 4402–4429. https://doi.org/10.1029/2018JA025387

Laundal, K. M., Gjerloev, J. W., Østgaard, N., Reistad, J. P., Haaland, S., Snekvik, K., et al. (2016). The impact of sunlight on high-latitude equivalent currents. *Journal of Geophysical Research: Space Physics*, *121*(3), 2715–2726. https://doi.org/10.1002/2015JA022236

Laundal, K. M., & Richmond, A. D. (2017). Magnetic coordinate systems. *Space Science Reviews*, *206*, 27–59. https://doi.org/10.1007/s11214-016-0275-y

Liou, K. (2010). Polar Ultraviolet Imager observation of auroral breakup. *Journal of Geophysical Research*, *115*(A12), A12219. https://doi.org/10.1029/2010JA015578

Liou, K., & Newell, P. T. (2010). On the azimuthal location of auroral breakup: Hemispheric asymmetry. *Geophysical Research Letters*, *37*(23), L23103. https://doi.org/10.1029/2010GL045537

Liou, K., Sotirelis, T., & Mitchell, E. (2020). Control of the east-west component of the interplanetary magnetic field on the occurrence of magnetic substorms. *Geophysical Research Letters*, *47*(5), e2020GL087406. https://doi.org/10.1029/2020GL087406

Liou, K., Sotirelis, T., & Richardson, I. (2018). Substorm occurrence and intensity associated with three types of solar wind structure. *Journal of Geophysical Research: Space Physics*, *123*(1), 485–496. https://doi.org/10.1002/2017JA024451

Li, H., Wang, C., & Peng, Z. (2013). Solar wind impacts on growth phase duration and substorm intensity: A statistical approach. *Journal of Geophysical Research: Space Physics*, *118*(7), 4270–4278. https://doi.org/10.1002/jgra.50399

McPherron, R. L. (1970). Growth phase of magnetospheric substorms. *Journal of Geophysical Research*, *75*(28), 5592–5599. https://doi.org/10.1029/JA075i028p05592

McPherron, R. L., & Chu, X. (2018). The midlatitude positive bay index and the statistics of substorm occurrence. *Journal of Geophysical Research: Space Physics*, *123*(4), 2831–2850. https://doi.org/10.1002/2017JA024766

McPherron, R. L., Hsu, T.-S., & Chu, X. (2015). An optimum solar wind coupling function for the AL index. *Journal of Geophysical Research: Space Physics*, *120*(4), 2494–2515. https://doi.org/10.1002/2014JA020619

McPherron, R. L., Russell, C. T., & Aubry, M. P. (1973). Satellite studies of magnetospheric substorms on August 15, 1968: 9. Phenomenological model for substorms. *Journal of Geophysical Research*, *78*(16), 3131–3149. https://doi.org/10.1029/JA078i016p03131

Milan, S. E., Gosling, J. S., & Hubert, B. (2012). Relationship between interplanetary parameters and the magnetopause reconnection rate quantified from observations of the expanding polar cap. *Journal of Geophysical Research*, *117*(A3), A03226. https://doi.org/10.1029/2011JA017082

Milan, S. E., Walach, M.-T., Carter, J. A., Sangha, H., & Anderson, B. J. (2019). Substorm onset latitude and the steadiness of magnetospheric convection. *Journal of Geophysical Research: Space Physics*, *124*(3), 1738–1752. https://doi.org/10.1029/2018JA025969

Morley, S. K., Koller, J., Welling, D. T., Larsen, B. A., Henderson, M. G., & Niehof, J. T. (2011). Spacepy - A Python-based library of tools for the space sciences. In *Proceedings of the 9th Python in science conference (SciPy 2010)*. Austin, TX.

Newell, P. T., & Gjerloev, J. W. (2011a). Evaluation of SuperMAG auroral electrojet indices as indicators of substorms and auroral power. *Journal of Geophysical Research*, *116*(A12), A12211. https://doi.org/10.1029/2011JA016779

Newell, P. T., & Gjerloev, J. W. (2011b). Substorm and magnetosphere characteristic scales inferred from the SuperMAG auroral electrojet indices. *Journal of Geophysical Research*, *116*(A12), A12232. https://doi.org/10.1029/2011JA016936

Newell, P. T., Gjerloev, J. W., & Mitchell, E. J. (2013). Space climate implications from substorm frequency. *Journal of Geophysical Research: Space Physics*, *118*(10), 6254–6265. https://doi.org/10.1002/jgra.50597

Newell, P. T., Liou, K., Gjerloev, J. W., Sotirelis, T., Wing, S., & Mitchell, E. J. (2016). Substorm probabilities are best predicted from solar wind speed. *Journal of Atmospheric and Solar-Terrestrial Physics*, *146*, 28–37. https://doi.org/10.1016/j.jastp.2016.04.019

Newell, P. T., Sotirelis, T., Liou, K., Meng, C.-I., & Rich, F. J. (2007). A nearly universal solar wind-magnetosphere coupling function inferred from 10 magnetospheric state variables. *Journal of Geophysical Research*, *112*(A1), A01206. https://doi.org/10.1029/2006JA012015

Nosé, M., Iyemori, T., Sugiura, M., & Slavin, J. A. (1995). A strong dawn/dusk asymmetry in Pc5 pulsation occurrence observed by the DE-1 satellite. *Geophysical Research Letters*, *22*(15), 2053–2056. https://doi.org/10.1029/95GL01794

Nosé, M., Iyemori, T., Wang, L., Hitchman, A., Matzka, J., Feller, M., et al. (2012). Wp index: A new substorm index derived from high-resolution geomagnetic field data at low latitude. *Space Weather*, *10*(8), S08002. https://doi.org/10.1029/2012SW000785

Nykyri, K., Ma, X., Dimmock, A., Foullon, C., Otto, A., & Osmane, A. (2017). Influence of velocity fluctuations on the Kelvin-Helmholtz instability and its associated mass transport. *Journal of Geophysical Research: Space Physics*, *122*(9), 9489–9512. https://doi.org/10.1002/2017JA024374

Ohma, A., Østgaard, N., Reistad, J. P., Tenfjord, P., Laundal, K. M., Moretto Jørgensen, T., et al. (2019). Observations of asymmetric lobe convection for weak and strong tail activity. *Journal of Geophysical Research: Space Physics*, *124*(12), 9999–10017. https://doi.org/10.1029/2019JA026773

Opgenoorth, H. J., Persson, M. A. L., Pulkkinen, T. I., & Pellinen, R. J. (1994). Recovery phase of magnetospheric substorms and its association with morning-sector aurora. *Journal of Geophysical Research*, *99*(A3), 4115–4129. https://doi.org/10.1029/93JA01502

Paschmann, G., Øieroset, M., & Phan, T. (2013). In situ observations of reconnection in space. *Space Science Reviews*, *178*, 385–417. https://doi.org/10.1007/s11214-012-9957-2

Paschmann, G., Papamastorakis, I., Baumjohann, W., Sckopke, N., Carlson, C. W., Sonnerup, B. U. Ö., et al. (1986). The magnetopause for large magnetic shear: AMPTE/IRM observations. *Journal of Geophysical Research*, *91*(A10), 11099. https://doi.org/10.1029/ja091ia10p11099

Perreault, P., & Akasofu, S.-I. (1978). A study of geomagnetic storms. *Geophysical Journal of the Royal Astronomical Society*, *54*(3), 547–573. https://doi.org/10.1111/j.1365-246X.1978.tb05494.x

Reistad, J. P., Laundal, K. M., Ohma, A., Moretto, T., & Milan, S. E. (2020). An explicit IMF B_y dependence on solar wind-magnetosphere coupling. *Geophysical Research Letters*, *47*(1), e2019GL086062. https://doi.org/10.1029/2019GL086062

Russell, C. T., & Brody, K. I. (1967). Some remarks on the position and shape of the neutral sheet. *Journal of Geophysical Research*, *72*(23), 6104–6106. https://doi.org/10.1029/JZ072i023p06104

Russell, C. T., & McPherron, R. L. (1973). Semiannual variation of geomagnetic activity. *Journal of Geophysical Research*, *78*(1), 92–108. https://doi.org/10.1029/JA078i001p00092

Sergeev, V. A., Pellinen, R. J., & Pulkkinen, T. I. (1996). Steady magnetospheric convection: A review of recent results. *Space Science Reviews*, *75*(3–4), 551–604. https://doi.org/10.1007/BF00833344

Sonnerup, B. U. Ö. (1974). Magnetopause reconnection rate. *Journal of Geophysical Research*, *79*(10), 1546–1549. https://doi.org/10.1029/JA079i010p01546

Takahashi, K., & Liou, K. (2004). Longitudinal structure of low-latitude Pi 2 pulsations and its dependence on aurora. *Journal of Geophysical Research*, *109*(A12), A12206. https://doi.org/10.1029/2004JA010580

Takahashi, K., Liou, K., & Yumoto, K. (2002). Correlative study of ultraviolet aurora and low-latitude pi2 pulsations. *Journal of Geophysical Research*, *107*(A12), 1417. https://doi.org/10.1029/2002JA009455

Tanskanen, E. I. (2009). A comprehensive high-throughput analysis of substorms observed by IMAGE magnetometer network: Years 1993–2003 examined. *Journal of Geophysical Research*, *114*(A5), A05204. https://doi.org/10.1029/2008JA013682

Tenfjord, P., & Østgaard, N. (2013). Energy transfer and flow in the solar wind-magnetosphere-ionosphere system: A new coupling function. *Journal of Geophysical Research: Space Physics*, *118*(9), 5659–5672. https://doi.org/10.1002/jgra.50545

Tsyganenko, N. A., & Fairfield, D. H. (2004). Global shape of the magnetotail current sheet as derived from Geotail and Polar data. *Journal of Geophysical Research*, *109*(A3), A03218. https://doi.org/10.1029/2003JA010062

Vasyliunas, V. M., Kan, J. R., Siscoe, G. L., & Akasofu, S.-I. (1982). Scaling relations governing magnetospheric energy transfer. *Planetary and Space Science*, *30*(4), 359–365. https://doi.org/10.1016/0032-0633(82)90041-1

Walsh, A. P., Haaland, S., Forsyth, C., Keesee, A. M., Kissinger, J., Li, K., et al. (2014). Dawn-dusk asymmetries in the coupled solar wind-magnetosphere-ionosphere system: A review. *Annales Geophysicae*, *32*(7), 705–737. https://doi.org/10.5194/angeo-32-705-2014

Weygand, J. M., McPherron, R., Kauristie, K., Frey, H., & Hsu, T.-S. (2008). Relation of auroral substorm onset to local al index and dispersionless particle injections. *Journal of Atmospheric and Solar-Terrestrial Physics*, *70*(18), 2336–2345. https://doi.org/10.1016/j.jastp.2008.09.030

Wild, J. A., Woodfield, E. E., & Morley, S. K. (2009). On the triggering of auroral substorms by northward turnings of the interplanetary magnetic field. *Annales Geophysicae*, *27*(9), 3559–3570. https://doi.org/10.5194/angeo-27-3559-2009

World Data Center for Geomagnetism, Kyoto, & Nosé, M. (2016). *Geomagnetic Wp index*. https://doi.org/10.17593/13437-46800

Yamaguchi, R., Kawano, H., Ohtani, S., Kokubun, S., & Yumoto, K. (2004). Total pressure variations in the magnetotail as a function of the position and the substorm magnitude. *Journal of Geophysical Research*, *109*(A3), A03206. https://doi.org/10.1029/2003JA010196

Yeoman, T. K., Freeman, M. P., Reeves, G. D., Lester, M., & Orr, D. (1994). A comparison of midlatitude Pi 2 pulsations and geostationary orbit particle injections as substorm indicators. *Journal of Geophysical Research*, *99*(A3), 4085–4093. https://doi.org/10.1029/93JA03233